Journal of Colloid and Interface Science 608 (2022) 3168–3177

Contents lists available at ScienceDirect

Journal of Colloid and Interface Science

journal homepage: www.elsevier.com/locate/jcis

Template-free construction of hollow mesoporous carbon spheres from a covalent triazine framework for enhanced oxygen electroreduction

Yong Zheng [a], Shan Chen [a], Kai A.I. Zhang [b,*], Jingyu Guan [c], Xiaohui Yu [a], Wei Peng [a], Hui Song [a], Jixin Zhu [e], Jingsan Xu [f], Xiaoshan Fan [a,*], Chao Zhang [a,*], Tianxi Liu [a,d]

[a] State Key Laboratory for Modification of Chemical Fibers and Polymer Materials, College of Materials Science and Engineering, Innovation Center for Textile Science and Technology, Donghua University, Shanghai 201620, PR China
[b] Department of Materials Science, Fudan University, Shanghai 200433, PR China
[c] State Key Laboratory of Chemical Resource Engineering, Beijing Key Laboratory of Electrochemical Process and Technology for Materials, Beijing University of Chemical Technology, Beijing 100029, PR China
[d] Key Laboratory of Synthetic and Biological Colloids, Ministry of Education, School of Chemical and Material Engineering, Jiangnan University, Wuxi 214122, PR China
[e] Shaanxi Institute of Flexible Electronics (SIFE), Northwestern Polytechnical University (NPU), 127 West Youyi Road, Xi'an 710072, PR China
[f] School of Chemistry, Physics and Mechanical Engineering, Queensland University of Technology, Brisbane, QLD 4001, Australia

HIGHLIGHTS

- A nitrogen, sulfur dual-doped hollow mesoporous carbon sphere (N/S-HMCS) is fabricated by a simple yet efficient template-free pyrolysis approach.
- The N/S-HMCS$_{900}$ exhibits high oxygen reduction reaction (ORR) activities with an excellent half-wave potential and high methanol tolerance.
- The optimal electrocatalyst can be used as air electrode materials in high-performance zinc-air batteries.
- Density functional theory (DFT) calculations reveal that N, S-dual dopant can create extra active sites with higher catalytic activity than the isolated *N*-dopant.

GRAPHICAL ABSTRACT

A template-free pyrolysis approach is proposed to fabricate nitrogen and sulfur doped hollow mesoporous carbon sphere (N/S-HMCS). The unique hollow/mesoporous nanostructure and abundant N, S-doped active sites prompt the optimal N/S-HMCS$_{900}$ exhibits satisfactory electrocatalysis in oxygen electroreduction for high-performance Zn-air battery.

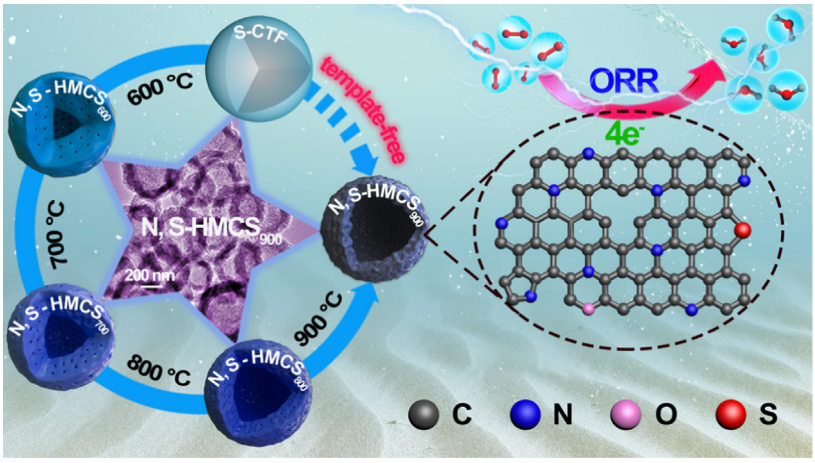

ARTICLE INFO

Article history:
Received 17 August 2021
Revised 9 November 2021
Accepted 10 November 2021
Available online 15 November 2021

Keywords:

ABSTRACT

The construction of hollow mesoporous carbon nanospheres (HMCS) avoiding the use of traditional soft/hard templates is highly desired for nanoscience yet challenging. Herein, we report a simple and straightforward template-free strategy for preparing nitrogen, sulfur dual-doped HMCSs (N/S-HMCSs) as oxygen reduction reaction (ORR) electrocatalysts. The unique hollow spherical and mesoporous structure was in-situ formed via a thermally initiated hollowing pathway from an elaborately engineered covalent triazine framework. Regulation of pyrolysis temperatures contributed to precisely tailoring of the shell thickness

* Corresponding authors.
E-mail addresses: kai_zhang@fudan.edu.cn (K.A.I. Zhang), xsfan@dhu.edu.cn (X. Fan), czhang@dhu.edu.cn (C. Zhang).

https://doi.org/10.1016/j.jcis.2021.11.048

Hollow mesoporous carbon nanospheres
Template-free
Covalent triazine framework
N
S-dual doping
Oxygen reduction reaction

of HMCSs. The resulting N/S-HMCS$_{900}$ (pyrolyzed at 900 °C) possessed high N and S contents, large specific surface areas, rich and uniform mesopores distribution. Consequently, as a metal-free ORR electrocatalyst, N/S-HMCS$_{900}$ exhibits a high half-wave potential, excellent methanol tolerance and great long-term durability. Additionally, density functional theory calculations demonstrate that N, S-dual dopant can create extra active sites with higher catalytic activity than the isolated *N*-dopant. This strategy provides new insights into the construction of hollow and mesoporous multi-heteroatom-doped carbon materials with tunable nanoarchitecture for various electrochemical applications.

1. Introduction

Hollow mesoporous carbon nanospheres (HMCS) featuring lightweight, adequate void space, high porosity and great conductivity are highly promising electrocatalytic materials for energy conversion and storage [1]. Hollow nanoarchitectures offer a multitude of advantages for applications over solid nanostructure species [2–5]. For instance, the large specific surface areas and open porous channels provide abundant active sites for various electrochemical redox reactions. The thin permeable shells greatly reduce the paths of fast ion and electron transport,[6] and the cavities afford additional volume for alleviating the strain and sufficient space for the electrolyte penetration [7]. Moreover, the complementary effects between the cavities and shells endow them with new meaningful properties, which are unavailable from the isolated components [8]. Until now, substantial efforts have been carried out to fabricate fuctional HMCS. In general, hollow architecture has been created through various hard or soft templates, such as SiO_2[9], polystyrene[10] and block copolymer[11], etc. Despite their tremendous success, the reported hard template methods are time-consuming, complicated and uneconomical caused by additional steps of the preparation and removal of templates [12]. Similarly, soft template approach is difficult to retain the robustness of hollow structures during the subsequent applications [13]. Thus, it remains a great challenge to develop an effective, safe and template-free method for preparing HMCSs.

Recently, covalent triazine frameworks (CTFs), a type of nitrogen-rich, porous organic polymer materials, have been widely applied in electrocatalysis and nanoscience fields due to their abundant heteroatom contents, controllable chemical structures, inherent rich micropores and large specific surface areas [14–16]. Annealing of CTFs is a prevailing strategy to gain versatile porous carbon materials with competitive electrochemical properties [17–19]. The rigid skeleton and excellent thermal stability of the CTFs ease the way to manipulate the exact content of doped heteroatoms in the carbon matrix, which would be almost impossible with conventional doping strategies. A variety of CTFs has been explored as ideal candidates to prepare heteroatom-doped carbons with desired micro/nanostructures for various applications [20,21,66]. Nevertheless, controllable synthesis of hollow carbon materials using CTFs has not yet been developed so far, and feasible synthetic strategies are highly desired.

Herein, we reported a simple yet efficient template-free strategy to prepare nitrogen and sulfur dual-doped hollow mesoporous carbon nanospheres (N/S-HMCS). A step-wise solvothermal polycondensation and subsequent carbonization were conducted by employing sulfur-bridged CTF sphere (S-CTF) as precursor. The key to this synthesis is to control the varieties of polymerization degrees in the interior and exterior layers of S-CTF. Via subsequent pyrolysis, the internal oligomers are critical to trigger the hollowing reaction to generate relatively large voids and rich mesopores in the derived N/S-HMCSs materials, containing atomically dispersed N and S atoms as accessible catalytic active sites. The optimal N/S-HMCS$_{900}$ possessed rich mesopores (~5 nm) distribution, high N and S contents (~6.1 and 1.3 at %) as well as large specific surface area (~331 $m^2\ g^{-1}$), exhibiting a superior ORR electrocatalytic activity and Zn-air battery performance compared with commercial Pt/C catalyst.

2. Experimental section

2.1. Chemicals

Cyanuric chloride (99.5 %) was obtained from Alfa aesar chemical Co., Ltd, China. Trithiocyanuric acid (95 %) and melamine (99 %) was purchased from Aladdin Reagent Co., Ltd, China. Acetonitrile (AR, ≥ 99.0 %) and ethanol (99.5 %) were purchased from Sinopharm Chemical Reagent Co., Ltd, China. Potassium hydroxide (GR, ≥ 90 %) and Nafion solution (5 wt%) were purchased from Sigma-Aldrich Co., Ltd.

2.2. Materials preparation

2.2.1. Synthesis of sulfur-bridged CTF(S-CTF) precursors:

Typically, cyanuric chloride (6 mmol, 1.10 g) and trithiocyanuric acid (6 mmol, 1.06 g) were fully dissolved in 30 mL of acetonitrile, respectively. Then the mixed solution was continuous stirred at 25 °C for 4 h, and transferred into the Teflon-lined stainless-steel autoclave, which was heated and maintained at 80 °C for 4 h and then at 160 °C for another 4 h. Afterward, the resultant was cool down to room temperature gradually. The obtained precipitates, denoted as S-CTF for simplicity, were filtered, washed with excess acetonitrile, ethanol, and deionized (DI) water for three times, respectively, and finally dried in a vacuum oven at 80 °C overnight. For comparison, sulfur-free precursors were prepared via a same process with sulfur-free melamine monomer, which was denoted as *N*-CTF.

2.2.2. Synthesis of N/S-HMCSs catalysts:

The S-CTF precursors were transferred to the ceramic crucible, and then pyrolyzed at a designed temperature for 2 h under continuous argon flow with a heating rate of 5 °C/min. Up cooling down naturally to room temperature, the as-obtained product was washed with DI water to remove unstable and inactive substances to obtain N/S-HMCS$_T$, where T represents the pyrolytic temperatures. As a convenient comparison, another catalyst was also pyrolyzed at 900 °C via the similar procedures with *N*-CTF as the precursor, named as N-HMCS$_{900}$.

3. Results and discussion

The synthetic route of N/S-HMCS is illustrated in scheme 1, involving a template-free hollowing process to generate a hollow spherical carbon skeleton. First, the heterogeneous solid spherical S-CTF precursor containing abundant pyridinic-N and S was

synthesized by a step-wise solvothermal polycondensation. Then, the as-synthesized S-CTF was pyrolyzed in an inert atmosphere under different temperatures to form the N/S-HMCSs with different shell thicknesses.

In the cross polarization/magic angle spinning (CP-MAS) ^{13}C nuclear magnetic resonance (NMR) spectroscopy of S-CTF, the main peak at 164 ppm is assigned to the triazine rings (Fig. S1a), while the shoulder peak at 157 ppm is attributed to the C atoms in the heteroatom-containing unit (N_2C-S) [23–25]. Fourier transform infrared spectrum (FT-IR) of S-CTF (Fig. S1b) showed signals at ~1520, ~1440, and ~1300 cm^{-1}, which are characteristic for the triazine rings in the S-CTF polymer framework [14,26,65]. The disappearance of the peaks at 850 cm^{-1} and 2542 cm^{-1} imply the absence of C-Cl bonds and S—H bands, further confirming the successful polycondensation of the S-CTF spheres through dehydrochlorination [27]. XPS survey spectra displayed in Fig. S2a indicates that the binding energies are corresponded to C, N and S atoms for different S-CTF sample, respectively. Meanwhile, the high-resolution N1s spectrum (Fig. S2b) has shown the peaks at 398.4 and 400.1 eV, which are attributed to pyridinic-N and N-$(C)_3$ structure [28,29]. Furthermore, XRD measurements of the S-CTF denote a diffraction pattern at around 27° corresponding to the stacking of the conjugated hexatomic heterocyclic systems (Fig. S3) [30]. Besides, the typical pattern of in-planar repeat packing at about 13° is not exhibited, indicating the disordered crystal structure of the polymeric precursors [31]. Also, the S-CTF polymer exhibited decent thermal stability, and thermal decomposition temperatures above 320 °C (Fig. S4).

Transmission electron microscope (TEM) images (Fig. 1a-c) showed that the as-obtained S-CTF precursor exhibits a solid spherical shape with an average diameter of 1.2 μm. In addition, similar regular spherical morphologies were observed in the sulfur-free *N*-CTF sample (Fig. S5a-b). After pyrolysis in an inert atmosphere at 900 °C, a surface-wrinkled spherical morphology was observed (Fig. 1d). It presented a hollow structure with a uniform shell thickness of ~ 70 nm and an inner cavity of ~ 250 nm, which might be due to the thermal-induced structural shrinkage and mass loss (Fig. 1e). Such hollow spherical morphologies were also obtained in the sulfur-free N-$HMCS_{900}$ (Fig. S5c-d). High-resolution TEM (HRTEM) image showed the presence of mesoporous pores in the shells of N/S-$HMCS_{900}$ (Fig. 1f). Fig. S6 displays the TEM images of the carbon spheres with different sizes of hollow cavities and shell thickness, which was formed by thermal treatment under distinct temperatures. It can be observed that with the increase of temperature, the hollow space of the carbon sphere increases gradually, while the shell thickness gradually decreases. This phenomenon demonstrates that the shell thickness of hollow carbon spheres can be accurately tuned by regulating the pyrolysis temperature.

Further, the HRTEM images and the selected area electron diffraction (SAED) pattern (inset of Fig. 1f) showed clear graphitic lattice fringes and weak diffraction rings, suggesting a certain graphitic property of the porous carbon shells [32]. Scanning TEM (STEM) images (Fig. 1g) further revealed that the hollow carbon spheres have a rough surface with a wrinkle-like structure, which can greatly improve the specific surface areas. Such nanowrinkles structures can facilitate the electrolyte's permeation, thus endowing the formed N/S-$HMCS_{900}$ with excellent electrocatalytic activity. The corresponding element mapping images (Fig. 1h-k) reveal that C, N, O and S atoms are uniformly distributed in the carbon shell, indicating commendable doping of N and S elements. Elemental mapping of O indicates the existence of some oxygen-containing functional groups.

Nitrogen adsorption/desorption isotherms of the N/S-$HMCS_{900}$ and N-$HMCS_{900}$ depicted representative type-IV curves with hysteresis loop at a high relative pressure (Fig. 2a and Fig. S7), meaning the existence of mesoporous structures [33]. The calculated specific surface area and total pore volume of the N/S-$HMCS_{900}$ (331 m^2 g^{-1}, 0.69 cm^3 g^{-1}) are much higher than these of N-$HMCS_{900}$ (179 m^2 g^{-1}, 0.27 cm^3 g^{-1}). The increased specific surface area of the N/S-$HMCS_{900}$ can provide more channels for electron and ion transmission, which is conducive to the improvement of electrochemical performance [34]. The pore size distribution of the N/S-$HMCS_{900}$ and N-$HMCS_{900}$ were centered at ~ 5 nm, confirmed the existence of uniformly distributed mesopore in the obtained HMCSs (inset of Fig. 2a and Fig. S7). These desirable mesopores are helpful for the transfer of reactants in the electrocatalytic process [35].

The X-ray diffraction (XRD) pattern of the N/S-$HMCS_{900}$ demonstrated two broad peaks assigning to the (002) and (100) diffraction modes at approximately 24.3°and 42.9°, confirming a disordered carbonaceous structure (Fig. S8a) [36]. Further, the Raman spectra corresponding to the graphitization degree of carbonaceous materials were shown in Fig. S8b. The intensity of the D band (1350 cm^{-1}) is higher than that of the G band (1590 cm^{-1}), indicating the existence of rich defects in the N/S-$HMCS_{900}$, which is beneficial to the exposure of electrocatalytic active sites [37,38].

The X-ray photoelectron spectroscopy (XPS) survey spectrum of the N/S-$HMCS_{900}$ presents typical peaks of C1s, N1s, O1s and S2p, proving the N and S elements were successfully doped into the carbon matrix (Fig. 2b) [39]. Especially, the corresponding content of C, N, O and S are 89.3, 6.1, 2.6 and 1.3 at%, respectively. Whereas, the XPS survey spectrum of the N-$HMCS_{900}$ exhibited characteristic peaks of C1s, N1s and O1s and the corresponding content are 91.2, 5.7 and 3.8 at%, respectively (Fig. S9). High resolution C1s XPS spectrum of the N/S-$HMCS_{900}$ (Fig. S10) shows the presence of C=C (284.5 eV), C—S/C=N (285.8 eV), C—N (287.1 eV), O-C=O

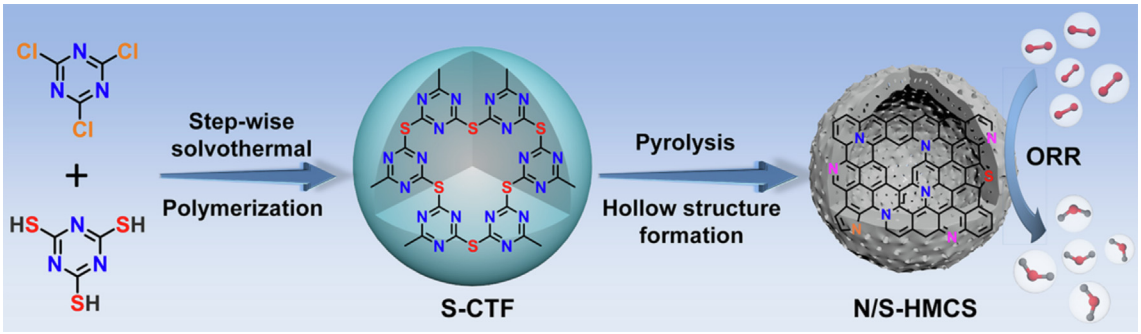

Scheme 1. The synthetic procedure of the N/S-HMCS via a template-free pathway.

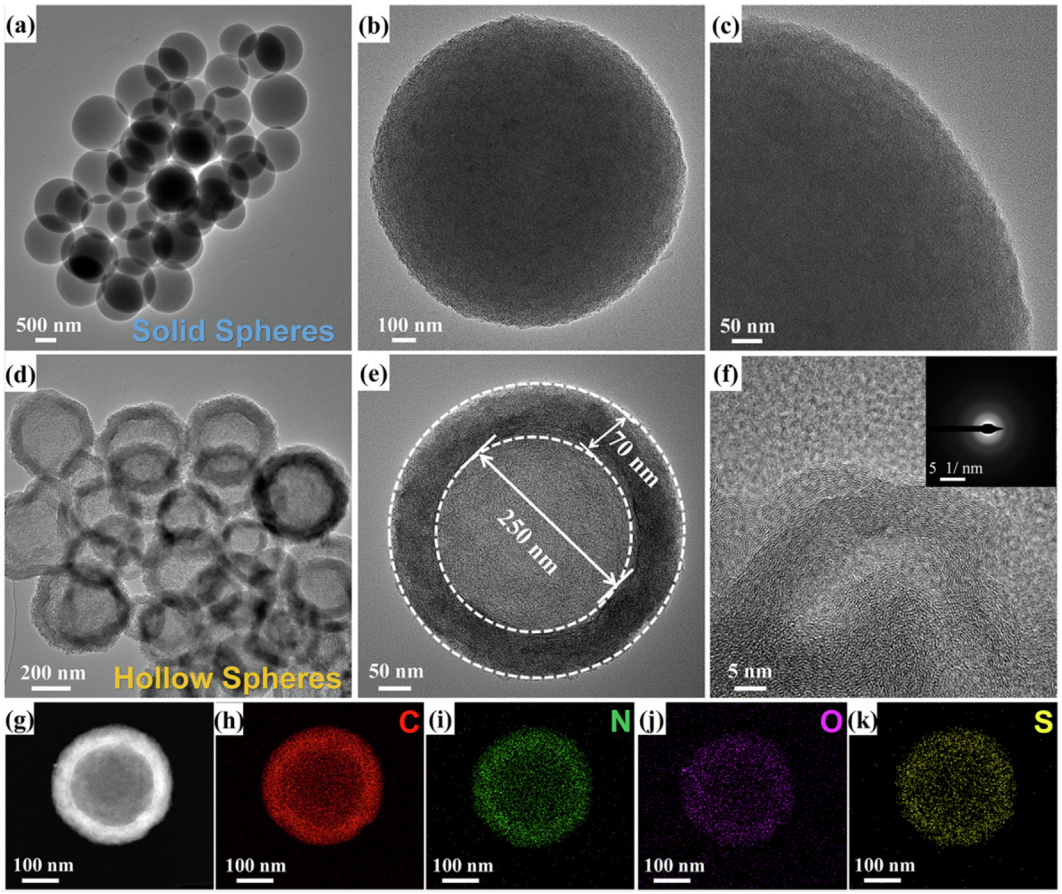

Fig. 1. (a-c) TEM images of S-CTF solid spheres; (d, e) TEM images, (f) High-resolution TEM (HRTEM), (g) STEM image and (h-k) corresponding EDS element (C, N, O, S) mappings of the N/S-HMCS$_{900}$.

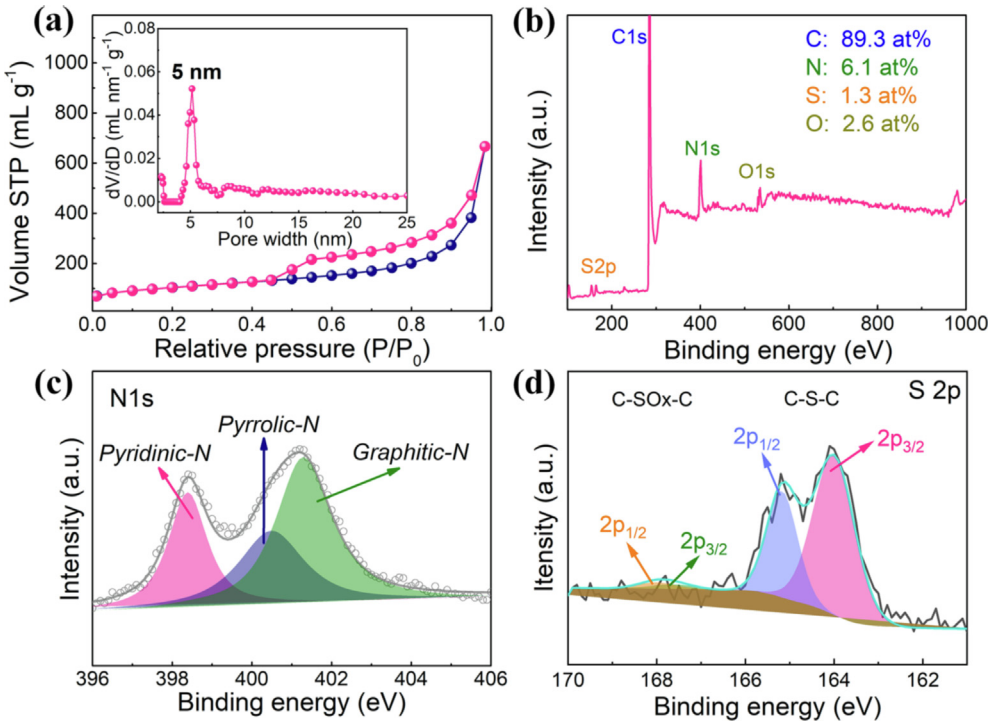

Fig. 2. (a) N_2 adsorption–desorption isotherms, (b) XPS survey spectrum, High-resolution (c) N1s and (d) S2p XPS spectra of N/S-HMCS$_{900}$. Inset of (a) showing the corresponding pore size distribution.

(288.6 eV) functional groups [40]. The N 1 s spectra can be deconvoluted into three peaks corresponding to pyridinic-N (398.3 eV), pyrrolic-N (400.5 eV) and graphitic N (401.3 eV) species, respectively (Fig. 2c) [41]. Fig. S11 shows that graphitic-N and pyridinic-N owns larger proportions among these *N*-doped forms, which are the significant active sites for electrocatalytic ORR [42]. A detailed scan of S 2p spectrum mainly decomposed into three different peaks, corresponding to carbon-bonded sulfur (C—S—C, 163.9 and 165.2 eV) and oxidized sulfur species (SOx, 167.4 and 168.1 eV), respectively (Fig. 2d) [43]. The introduction of S element imparts structural defects and a favorable electronic structure owing to the larger radius of S atom, which provides abundant electrocatalytic active sites for the ORR [44]. The content of C, N and S elements in the N/S-HMCS$_{900}$ are further confirmed by the elemental analysis to be 85.6, 5.8 and 1.1 at %, respectively, which is well consistent with the XPS results (Fig. S12). As a comparison, the content of C and N elements in the N-HMCS$_{900}$ are 87.1 and 5.3 at %, respectively. The relatively high nitrogen and sulfur contents in N/S-HMCS$_{900}$ are in favor of its electrocatalytic activity [45].

The time and reaction temperature effects on the formation of S-CTF were investigated in detail. Spherical nanostructure was synthesized using a one-pot solvothermal process involving three stepwise reaction stages. The SEM images of the intermediates at different temperature stages (25 °C, 80 °C, 160 °C) and varied intervals (0, 4, 8, and 12 h) are shown in Fig. S13. Specifically, the oligomer nanoparticles with a size of ~ 100 nm were formed after room-temperature reaction for 4 h. With the extension of reaction time, these nanoparticles tend to aggregate to form irregular spheres. After another 4 h at 80 °C, these nanoparticles evolved into well-defined spheres through further aggregation and assembly. When the reaction temperature was further increased to 160 °C for the last 4 h, a more compact and regular structure was discovered. Based on the above observations, a versatile step-wise polycondensation route for the formation of S-CTF from the predesigned organic monomers is proposed. Firstly, low cross-linked oligomers were formed and tended to be nucleated directly to grow into larger particles at the initial stage of relative low-temperature polycondensation. With the increase of reaction temperature, these oligomers immediately aggregate and further deep polycondensation occurred between the residual active groups, forming small irregular spheres. By further increasing the solvothermal temperature, solid spheres with increased diameter were formed by the deeply-crosslinking ripeness process. Therefore, the internal structure of S-CTF is composed of oligomers, while the exterior space is a highly cross-linked polymer.

Based on the internal and external heterogeneity of S-CTF, we provide a thermally initiated hollowing mechanism for the formation of the resultant N/S-HMCSs. During this procedure, the central oligomers with a relatively lower polymerization degree showed a strong tendency to decompose and volatile, and then subsequently migrated to the shell by redeposition, thus leading to the formation of hollow interior spaces. Meanwhile, the outer polymer shell as a surface-protected layer was in-situ carbonized into a stabilized carbon shell. The morphological evolution process was observed through ex-situ TEM images, and different temperature stages were used to simulate the various stages of the formation of hollow structures (Fig. 3). The center of the sphere started to become hollow at a pyrolysis temperature of 500 °C, when the precursor began to decompose. The gas produced by thermal decomposition in the internal layer migrated out gradually to maintain a stable structure with reduced surface energies, thus finally forming the hollow cavities inside the spheres. The further increase in temperature led to further decomposition from the core, and the diameter of the cavity gradually increased, making the appearance of hollow structures more pronounced. During this process, the shell was carbonized to form the carbon shell framework, while the inner core was further transferred to the shell as nitrogen and sulfur sources to realize in-situ doping of N and S. The average diameters are ~ 1050, 850, 700, and 450 nm for the N/S-HMCS$_{500}$, N/S-HMCS$_{600}$, N/S-HMCS$_{700}$ and N/S-HMCS$_{800}$, respectively (Fig. 3). Simultaneously, the generated gas should etch the remaining

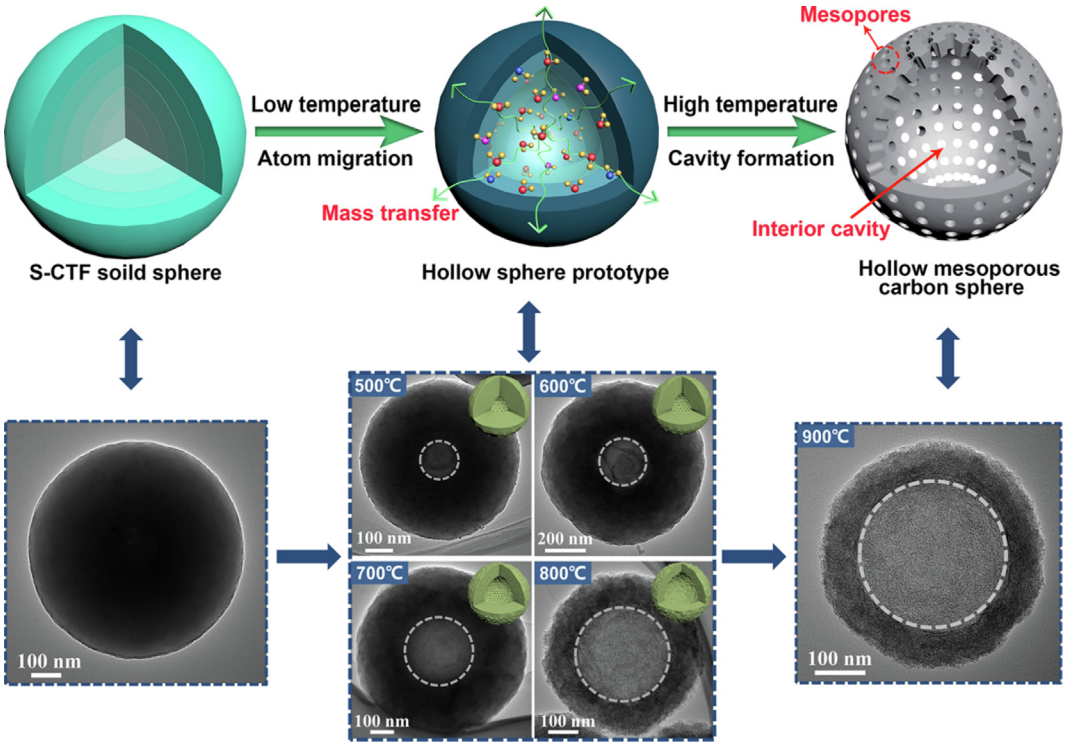

Fig. 3. Proposed formation process of N/S-HMCS by the thermally initiated hollowing mechanism with corresponding TEM images.

carbon shell, producing numerous mesopores and making the surface rougher. The specific surface areas of S-CTF, N/S-HMCS$_{500}$, N/S-HMCS$_{600}$, N/S-HMCS$_{700}$, N/S-HMCS$_{800}$ and N/S-HMCS$_{900}$ are 6, 12, 17, 54, 220 and 331 $m^2\ g^{-1}$, respectively (Fig. S14 and Table 1). These results indicate that the increased cavity volume enlarges the specific surface areas. The current hollowing process occurred preferentially in the spherical interior rather than the shell due to their inherent structure difference between the interior and the exterior of S-CTF. Thermal shrinkage of the external shell leads to the decrease of HMCS diameters, while the increasing void volume ascribed to the increase of pyrolysis temperature enhanced the decomposition of the internal oligomer further.

The electrocatalytic activity of the resultant N/S-HMCS$_{900}$ toward ORR was evaluated by cyclic voltammetry (CV) measurements in O_2 and N_2-saturated 0.1 M KOH solution, respectively (Fig. S15). The typical cathodic ORR peaks at the potential of ~ 0.79 V vs. RHE were observed in O_2-saturated electrolyte, while no peaks were presented in N_2-saturated electrolyte, predicting that N/S-HMCS$_{900}$ possessed outstanding ORR activities [46]. The onset potential and half-wave potential (Fig. 4a) was close to that of Pt/C catalyst and exceeding other prepared catalysts and most of the other reported catalysts (Fig. S16 and Table S1) [47]. Besides, the N/S-HMCS$_{900}$ performed a low Tafel slope of 72 mV dec^{-1}, even smaller than that of Pt/C catalyst (75 mV dec^{-1}) displayed in Fig. S17, suggesting outstanding electrocatalytic kinetics [48]. Linear sweep voltammetry (LSV) results illustrated that the limiting current density of the N/S-HMCS$_{900}$ electrode increased with the rise of rotation rates from 800 to 2400 rpm (Fig. 4b). The corresponding Koutecky-Levich (K-L) plots displayed perfect linearity and parallelism under different potentials (Fig. 4c). From the K-L equation, the average electron transfer number (n) was calculated to be ~ 3.95 (Fig. 4d), indicating a nearly four-electron transfer pathway for ORR. Rotating ring disk electrode (RRDE) measurements revealed that the N/S-HMCS$_{900}$ possesses a low H_2O_2 yield (<10 %) and an average n of ~ 3.97, matching well with the results of K-L plots (Fig. S18). In addition, the C_{dl} of the as-obtained catalysts are also measured by CV analysis (Fig. S19a-b). As a result, N/S-HMCS$_{900}$ also showed much higher C_{dl} value (16.7 mF cm^{-2}) than that of N-HMCS$_{900}$ (2.7 mF cm^{-2}) in 0.1 M KOH (Fig. S19c). The significant increase of ECSA may result in the enhancement of electrocatalytic activity. After a continuous operation for 10 h, the current density was maintained at ~ 97.8 % while Pt/C catalysts only reserved ~ 87.4%, indicating the superior durability (Fig. 4f) [25]. Besides, methanol tolerance is another significant factor in practical application. After adding 1 M methanol in the electrolyte at 200 s, no noticeable change happened in the N/S-HMCS$_{900}$ catalyst, whereas an obvious response was observed for Pt/C catalyst (Fig. 4e). The superior ORR electrocatalytic performance was ascribed to the unique hollow architecture, rich mesopores and high density of N, S-doped heteroatom active sites [49]. To further investigate the surface-evolution process of the N/S-HMCS$_{900}$ catalyst during the ORR process, we also characterized and analyzed the morphology and composition of the N/S-HMCS$_{900}$ catalyst after long-term running test. TEM observation demonstrated the microstructure is basically unchanged after the stability test (as shown in Fig. S20a-c). Corresponding elemental mapping images (Fig. S20d-g) revealed that C, N and S elements still exist and homogeneously distribute in the carbon framework, suggesting that the as-made catalyst has great structural stability. Fig. S21a exhibits the XPS spectrum of N/S-HMCS$_{900}$ after the stability test. The peaks of O 1 s increased significantly, which might be ascribed to the slight oxidation of carbon matrix during long-term test

Table 1
Structure parameters of pyrolytic S-CTF under different temperatures.

Sample	BET ($m^2\ g^{-1}$)	Total pore volume ($cm^3\ g^{-1}$)	Mesopore volume ($cm^3\ g^{-1}$)
S-CTF	6	0.01	0.01
N/S-HMCS$_{500}$	12	0.03	0.03
N/S-HMCS$_{600}$	17	0.07	0.06
N/S-HMCS$_{700}$	54	0.15	0.14
N/S-HMCS$_{800}$	220	0.32	0.16
N/S-HMCS$_{900}$	331	0.69	0.64
N-HMCS$_{900}$	179	0.27	0.25

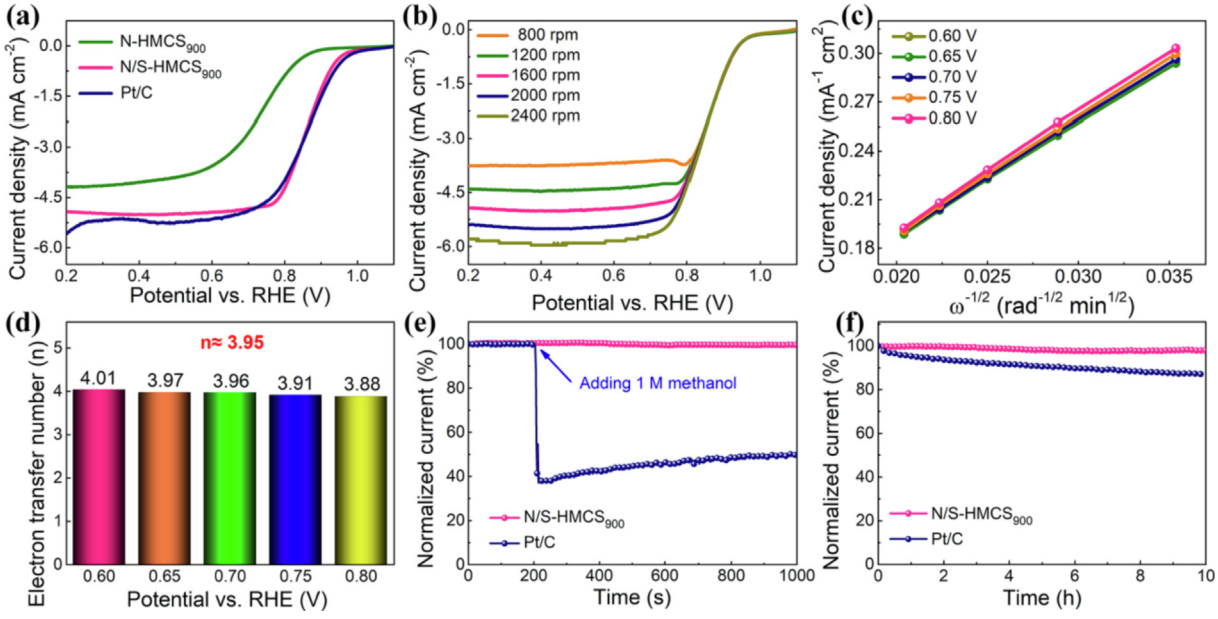

Fig. 4. (a) LSV curves of N-HMCS$_{900}$, N/S-HMCS$_{900}$ and Pt/C electrodes at a rotation rate of 1600 rpm; (b) LSV curves of the N/S-HMCS900 at various rotating speeds; (c) K-L plots the N/S-HMCS$_{900}$ at various potentials; (d) The electron transfer number of the N/S-HMCS$_{900}$ at 0.6–0.8 V; (e) Chronoamperometric responses of N/S-HMCS$_{900}$ and Pt/C catalysts in O_2-saturated 0.1 M KOH; (f) Current-time (i-t) chronoamperometric responses of N/S-HMCS$_{900}$ and Pt/C catalysts by adding 1 M methanol after 200 s in O_2-satuated 0.1 M KOH.

process. Moreover, after the stability test, the corresponding N 1 s and S 2p spectra changed slightly (Fig. S21b-c), indicating that the carbon matrix has decent chemical stability.

To evaluate the practical applications of electrocatalysts, we assembled a primary Zn-air battery using the N/S-HMCS$_{900}$ as a cathode material (Fig. 5a). Fig. 5b shows the as-assembled battery

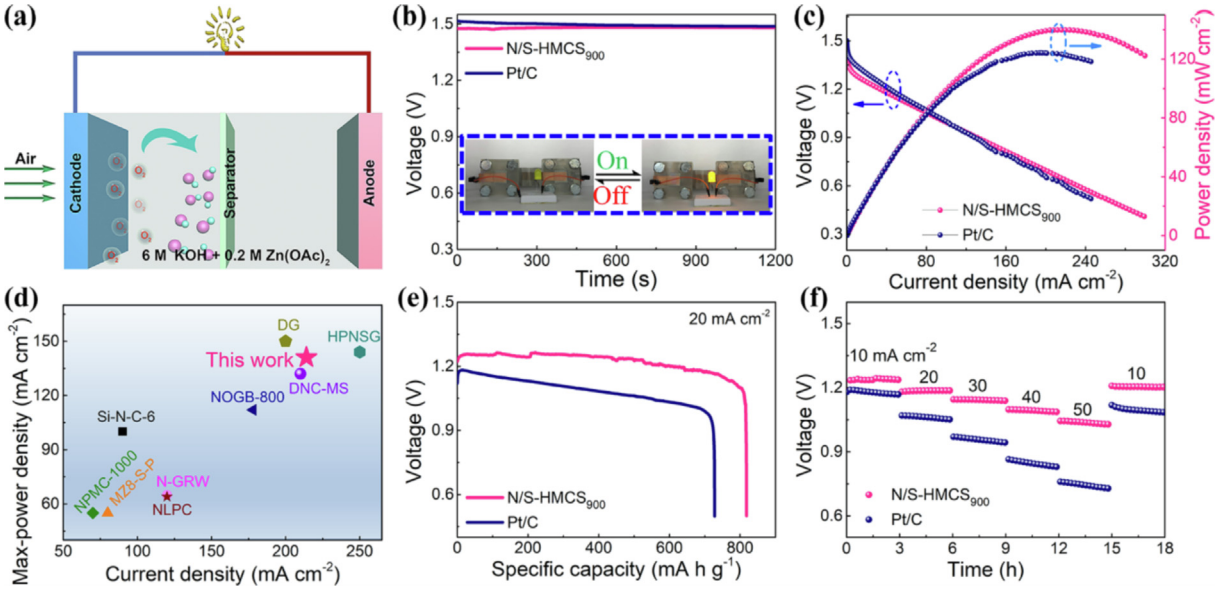

Fig. 5. (a) Schematic illustration of a primary Zn-air battery with an N/S-HMCS$_{900}$ cathode. (b) Open circuit voltage curves of the as-assemble Zn-air battery with the N/S-HMCS$_{900}$ and Pt/C air electrode, respectively; Inset of (d) is the LED light powered through two primary Zn-air batteries; (c) Polarization curves and power densities of N/S-HMCS$_{900}$ and Pt/C cathodes, respectively; (d) Performance comparisons of power density of N/S-HMCS$_{900}$ with other catalysts in the literature[53–61]; (e) Galvanostatic discharge curves of Zn-air batteries with the N/S-HMCS$_{900}$ and Pt/C cathodes at 20 mA cm^{-2}; (f) Rate performance of N/S-HMCS$_{900}$ and Pt/C electrodes at a current density of 10, 20, 30, 40, 50, and 10 mA cm^{-2}, respectively.

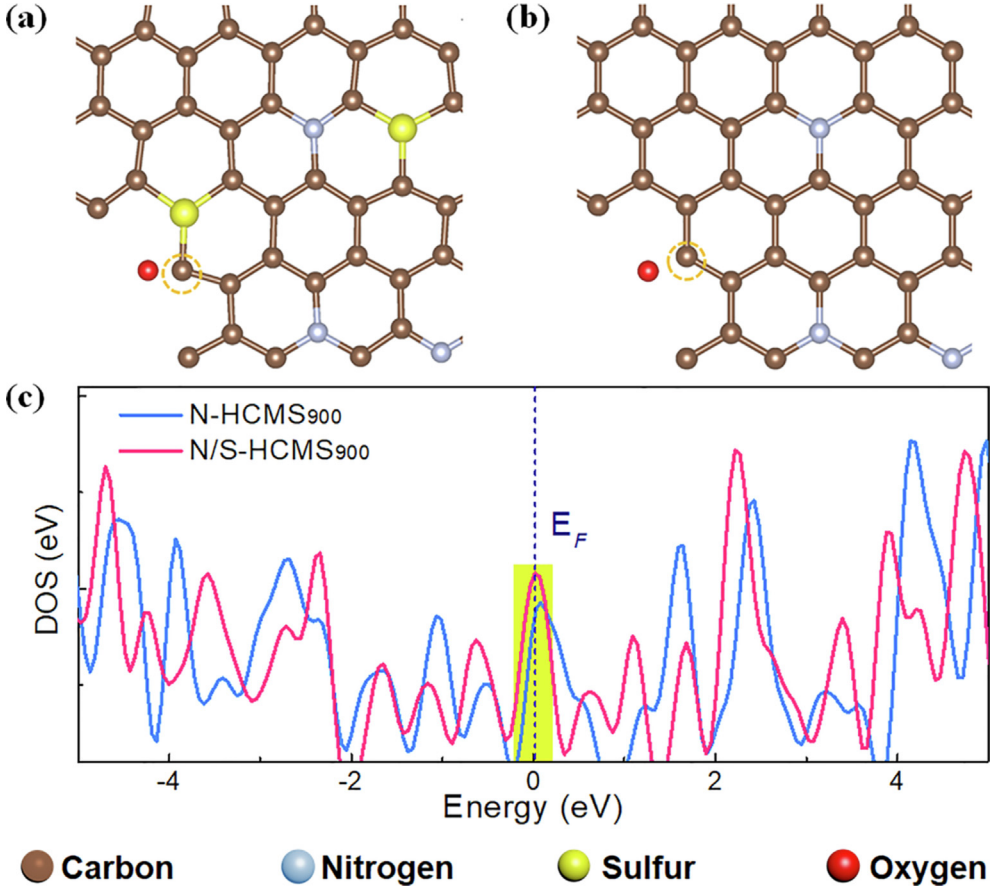

Fig. 6. Optimized structures for the stable adsorbed O atom on (a) N-HMCS$_{900}$ and (b) N/S-HMCS$_{900}$; (c) the DOS plots of N-HMCS$_{900}$ and N/S-HMCS$_{900}$.

has a continuous steady open circuit voltage at ~ 1.47 V, which is very close to that of Pt/C catalyst (~1.51 V) [50]. Two Zn-air batteries fabricated by using the N/S-$HMCS_{900}$ cathode are capable of lighting up a LED lamp for a long time, indicating that N/S-$HMCS_{900}$ can satisfy the requirements in practical applications. Noticeably, from the polarization curve, N/S-$HMCS_{900}$ showed a high peak power density of ~ 141 mW cm^{-2}, exceeding that of Pt/C catalyst (~123 mW cm^{-2}) and most of the reported catalysts (Fig. 5c-d) [51]. As dispalyed in Fig. 5e, the N/S-$HMCS_{900}$-catalyzed Zn-air battery delivered a stable discharge voltage (greater than1.2 V) almost without obvious degradation when galvanostatically discharged at 20 mA cm^{-2}. The specific capacity of the battery assembled by N/S-$HMCS_{900}$ at the discharge current density of 20 mA cm^{-2} is more than 800 mAh g_{Zn}^{-1} (normalized to the mass of consumed Zn plate), which is much higher than that of Pt/C-catalyzed Zn-air battery [52]. Furthermore, the self-made Zn-air battery utilizing N/S-$HMCS_{900}$ electrode also exhibited superior rate performance than that of the commercial Pt/C-based electrode (Fig. 5f). Notably, the N/S-$HMCS_{900}$-based air electrode also displayed superior performance compared to other carbon-based air electrodes reported in the previous literature (Table S2). Above results clearly demonstrate that our developed N/S-$HMCS_{900}$ electrocatalyst is a highly competitive candidate to substitute commercial Pt/C catalyst for practical application in energy conversation fields.

To investigate the effects of the sulfur doping in N/S-$HMCS_{900}$ toward the ORR activity, density functional theory (DFT) calculations were carried out to study the adsorption energy of different heteroatom-doped carbon models. The specific configurations of N/S-$HMCS_{900}$ structures are depicted in Fig. 6a-b. The edge C atoms adjacent to the S atoms are found to be the active centers toward ORR, which is beneficial to the adsorption of O atom [62]. By comparing the charge density differences, we found that the electrons of carbon framework were attracted to the S-doped ORR catalytic active sites (Fig. S22). Additionally, the conductivity of t N-$HMCS_{900}$ and N/S-$HMCS_{900}$ models was also predicted by the density of states (DOS), which is important for enabling catalysts with faster electron transport capability [63]. As shown in Fig. 6c, the DOS of the N/S-$HMCS_{900}$ exhibit a relatively higher electron density at the Fermi energy (E_F) than the *N*-doped nanocarbon models. It indicates that efficiently sulfur doping plays an important role in enhancing the conductivity of N/S-$HMCS_{900}$,[64] which is also confirmed by corresponding conductivity test (Table S3). All of those computational results reveal that the extra sulfur doping indeed makes a significant improvement to the electrochemical ORR activity of the resultant electrocatalysts.

4. Conclusion

In summary, a thermally initiated hollowing strategy is employed to prepare nitrogen, sulfur dual-doped hollow mesoporous carbon spheres (N/S-HMCS) using a sulfur-bridged CTF solid spheres (S-CTF) as precursor. Controlling the polymerization degrees in the interior and exterior layers of S-CTF polymer ensured the formation of the hollow nanostructure without any templates and the shell thickness can be precisely tailored by regulating the pyrolysis temperatures. As a result, the optimal N/S-$HMCS_{900}$ exhibited a unique hollow and mesoporous structure with desired shell thickness (~70 nm), uniform mesopores (~5 nm), large specific surface area (~331 m^2 g^{-1}) and high-content heteroatom doping (~6.1 and 1.3 at% for nitrogen and sulfur, respectively). These distinctive characteristics enabled N/S-$HMCS_{900}$ with high electrocatalytic activity and great durability towards the ORR and Zn-air batteries. Furthermore, DFT calculations is helpful to illuminate the contribution of N, S dual-doping to the enhanced ORR performance. This study demonstrates a promising template-free method toward the synthesis of hollow mesoporous carbon materials with precisely tailored structures, which has a great potential for energy-related electrocatalytic applications.

CRediT authorship contribution statement

Yong Zheng: synthesized the materials, carried out the experimental work, wrote the manuscript, conceived the project idea and revised the manuscript. **Shan Chen:** conceived the project idea and revised the manuscript. **Kai A. I. Zhang:** revised the manuscript. Jingyu Guan helped out in calculation. **Xiaohui Yu, Wei Peng and Hui Song:** assisted in the characterization and synthesized the materials. **Jixin Zhu and Jingsan Xu:** revised the manuscript. **Xiaoshan Fan, Chao Zhang and Tianxi Liu:** supervised the project. All authors discussed the results and commented on the manuscript.

Declaration of Competing Interest

The authors declare that they have no known competing financial interests or personal relationships that could have appeared to influence the work reported in this paper.

Acknowledgments

The authors are grateful for the financial support from the National Natural Science Foundation of China (51773035), the Shanghai Rising-Star Program (18QA1400200), and the Shanghai Scientific and Technological Innovation Project (18JC1410600).

Appendix A. Supplementary material

Supplementary data to this article can be found online at https://doi.org/10.1016/j.jcis.2021.11.048.

References

[1] G. Zheng, S.W. Lee, Z. Liang, H.-W. Lee, K. Yan, H. Yao, H. Wang, W. Li, S. Chu, Y.i. Cui, Interconnected hollow carbon nanospheres for stable lithium metal anodes, Nat. Nanotechnol. 9 (8) (2014) 618–623.
[2] J. Park, T. Kwon, J. Kim, H. Jin, H.Y. Kim, B. Kim, S.H. Joo, K. Lee, Hollow nanoparticles as emerging electrocatalysts for renewable energy conversion reactions, Chem. Soc. Rev. 47 (22) (2018) 8173–8202.
[3] T. Wang, C. Yang, Y. Liu, M. Yang, X. Li, Y. He, H. Li, H. Chen, Z. Lin, Dual-Shelled Multidoped Hollow Carbon Nanocages with Hierarchical Porosity for High-Performance Oxygen Reduction Reaction in Both Alkaline and Acidic Media, Nano Lett. 20 (8) (2020) 5639–5645.
[4] W. Li, D. Wang, Z. Song, Z. Gong, X. Guo, J. Liu, Z. Zhang, G. Li, Carbon confinement synthesis of interlayer-expanded and sulfur-enriched MoS_{2+x} nanocoating on hollow carbon spheres for advanced Li-S batteries, Nano Res. 12 (11) (2019) 2908–2917.
[5] X. Yu, Y. Zheng, H. Zhang, Y. Wang, X. Fan, T. Liu, Fast-Recoverable, Self-Healable, and Adhesive Nanocomposite Hydrogel Consisting of Hybrid Nanoparticles for Ultrasensitive Strain and Pressure Sensing, Chem. Mater. 33 (15) (2021) 6146–6157.
[6] J. Zhu, H. Zhou, C. Zhang, J. Zhang, S. Mu, Dual active nitrogen doped hierarchical porous hollow carbon nanospheres as an oxygen reduction electrocatalyst for zinc-air batteries, Nanoscale 9 (35) (2017) 13257–13263.
[7] D.-S. Bin, Z.-X. Chi, Y. Li, K.e. Zhang, X. Yang, Y.-G. Sun, J.-Y. Piao, A.-M. Cao, L.-J. Wan, Controlling the compositional chemistry in single nanoparticles for functional hollow carbon nanospheres, J. Am. Chem. Soc. 139 (38) (2017) 13492–13498.
[8] X. Zhu, Y. Xia, X. Zhang, A.A. Al-Khalaf, T. Zhao, J. Xu, L. Peng, W.N. Hozzein, W. Li, D. Zhao, Synthesis of carbon nanotubes@mesoporous carbon core-shell structured electrocatalysts via a molecule-mediated interfacial co-assembly strategy, J. Mater. Chem. A 7 (15) (2019) 8975–8983.
[9] R. Du, W. Yi, W. Li, H. Yang, H. Bai, J. Li, G. Xi, Quasi-metal Microwave Route to MoN and Mo_2C Ultrafine Nanocrystalline Hollow Spheres as Surface-Enhanced Raman Scattering Substrates, ACS Nano 14 (10) (2020) 13718–13726.
[10] A.F. Arif, Y. Kobayashi, E.M. Schneider, S.C. Hess, R. Balgis, T. Izawa, H. Iwasaki, S. Taniguchi, T. Ogi, K. Okuyama, W.J. Stark, Selective low-energy carbon

dioxide adsorption using monodisperse nitrogen-rich hollow carbon submicron spheres, Langmuir 34 (1) (2018) 30–35.
[11] Y. Li, H. Tan, R.R. Salunkhe, J. Tang, L.K. Shrestha, B.P. Bastakoti, H. Rong, T. Takei, J. Henzie, Y. Yamauchi, K. Ariga, Hollow carbon nanospheres using an asymmetric triblock copolymer structure directing agent, Chem. Commun. 53 (1) (2017) 236–239.
[12] L.e. Yu, H.B. Wu, X.W.D. Lou, Self-templated formation of hollow structures for electrochemical energy applications, Accounts Chem. Res. 50 (2) (2017) 293–301.
[13] Y. Liu, Z. Wang, W. Teng, H. Zhu, J. Wang, A.A. Elzatahry, D. Al-Dahyan, W. Li, Y. Deng, D. Zhao, A template-catalyzed in situ polymerization and co-assembly strategy for rich nitrogen-doped mesoporous carbon, J. Mater. Chem. A 6 (7) (2018) 3162–3170.
[14] P. Kuhn, M. Antonietti, A. Thomas, Porous, covalent triazine-based frameworks prepared by ionothermal synthesis, Angew. Chem. Int. Edit. 47 (18) (2008) 3450–3453.
[15] S. Ren, M.J. Bojdys, R. Dawson, A. Laybourn, Y.Z. Khimyak, D.J. Adams, A.I. Cooper, Porous, fluorescent, covalent triazine-based frameworks via room-temperature and microwave-assisted synthesis, Adv. Mater. 24 (17) (2012) 2357–2361.
[16] B. Zhang, X. Zhang, K. Wan, J. Zhu, J. Xu, C. Zhang, T. Liu, Dense Hydrogen-Bonding Network Boosts Ionic Conductive Hydrogels with Extremely High Toughness, Rapid Self-Recovery, and Autonomous Adhesion for Human-Motion Detection, Research 2021 (2021) 9761625.
[17] J. Zhu, J. Yang, Z. Xu, J. Wang, Y. Nuli, X. Zhuang, X. Feng, Silicon anodes protected by a nitrogen-doped porous carbon shell for high-performance lithium-ion batteries, Nanoscale 9 (25) (2017) 8871–8878.
[18] M.M. Vadiyar, X. Liu, Z. Ye, Macromolecular polyethynylbenzonitrile precursor-based porous covalent triazine frameworks for superior high-rate high-energy supercapacitors, ACS Appl. Mater. Interfaces 11 (49) (2019) 45805–45817.
[19] L. Yang, X. Zhou, Z. Jia, H. Lv, Y. Zhu, J. Liu, Z. Yang, Selective tailoring of covalent bonds on graphitized hollow carbon spheres towards controllable porous structure and wideband electromagnetic absorption, Carbon 167 (2020) 843–851.
[20] L. Jiao, Y. Hu, H. Ju, C. Wang, M.-R. Gao, Q. Yang, J. Zhu, S.-H. Yu, H.-L. Jiang, From covalent triazine-based frameworks to N-doped porous carbon/reduced graphene oxide nanosheets: efficient electrocatalysts for oxygen reduction, J. Mater. Chem. A 5 (44) (2017) 23170–23178.
[21] H. Liang, X. Zhuang, S. Brüller, X. Feng, K. Müllen, Hierarchically porous carbons with optimized nitrogen doping as highly active electrocatalysts for oxygen reduction, Nat. Commun. 5 (2014) 4973–4979.
[23] S. Guo, P. Yang, Y. Zhao, X. Yu, Y. Wu, H. Zhang, B. Yu, B. Han, M.W. George, Z. Liu, Direct Z-scheme heterojunction of SnS_2/sulfur-bridged covalent triazine frameworks for visible-light-driven CO_2 photoreduction, ChemSusChem 13 (9) (2020) 1–7.
[24] Y. Cui, Z. Ding, X. Fu, X. Wang, Construction of conjugated carbon nitride nanoarchitectures in solution at low temperatures for photoredox catalysis, Angew. Chem. Int. Edit. 51 (47) (2012) 11814–11818.
[25] Y. Zheng, H. Song, S. Chen, X. Yu, J. Zhu, J. Xu, K.A.I. Zhang, C. Zhang, T. Liu, Metal-free multi-heteroatom-doped carbon bifunctional electrocatalysts derived from a covalent triazine polymer, Small 16 (47) (2020) 2004342, https://doi.org/10.1002/smll.v16.4710.1002/smll.202004342.
[26] L. Hao, J. Ning, B. Luo, B. Wang, Y. Zhang, Z. Tang, J. Yang, A. Thomas, L. Zhi, Structural Evolution of 2D Microporous Covalent Triazine-Based Framework toward the Study of High-Performance Supercapacitors, J. Am. Chem. Soc. 137 (1) (2015) 219–225.
[27] D.C. Jones, C.M. Carr, W.D. Cooke, D.M. Lewis, Investigating the Photo-Oxidation of Wool Using FT-Raman and FT-IR Spectroscopies, Text. Res. J. 68 (10) (1998) 739–748.
[28] Y. Kang, Y. Yang, L.-C. Yin, X. Kang, L. Wang, G. Liu, H.-M. Cheng, Selective Breaking of Hydrogen Bonds of Layered Carbon Nitride for Visible Light Photocatalysis, Adv. Mater. 28 (30) (2016) 6471–6477.
[29] S. Chen, Y. Zheng, B. Zhang, Y. Feng, J. Zhu, J. Xu, C. Zhang, W. Feng, T. Liu, Cobalt, nitrogen-doped porous carbon nanosheet-assembled flowers from metal-coordinated covalent organic polymers for efficient oxygen reduction, ACS Appl. Mater. Interfaces 11 (1) (2019) 1384–1393.
[30] X. Zhu, C. Tian, S.M. Mahurin, S.-H. Chai, C. Wang, S. Brown, G.M. Veith, H. Luo, H. Liu, S. Dai, A Superacid-Catalyzed Synthesis of Porous Membranes Based on Triazine Frameworks for CO_2 Separation, J. Am. Chem. Soc. 134 (25) (2012) 10478–10484.
[31] L. Zhu, Y. Zhu, Y. Pan, Y. Huang, X. Huang, X. Tang, Fully crosslinked poly [cyclotriphosphazene-co-(4,4'-sulfonyldiphenol)] microspheres via precipitation polymerization and their superior thermal properties, Macromol. React. Eng. 42 (5) (2007) 835–845.
[32] W. Ren, X. Tan, W. Yang, C. Jia, S. Xu, K. Wang, S.C. Smith, C. Zhao, Isolated Diatomic Ni-Fe Metal-Nitrogen Sites for Synergistic Electroreduction of CO_2, Angew. Chem., Int. Ed. 58 (21) (2019) 6972–6976.
[33] L. Peng, C.-T. Hung, S. Wang, X. Zhang, X. Zhu, Z. Zhao, C. Wang, Y. Tang, W. Li, D. Zhao, Versatile nanoemulsion assembly approach to synthesize functional mesoporous carbon nanospheres with tunable pore sizes and architectures, J. Am. Chem. Soc. 141 (17) (2019) 7073–7080.
[34] S. Liu, J. Xu, J. Zhu, Y. Chang, H. Wang, Z. Liu, Y. Xu, C. Zhang, T. Liu, Leaf-inspired interwoven carbon nanosheet/nanotube homostructures for supercapacitors with high energy and power densities, J. Mater. Chem. A 5 (37) (2017) 19997–20004.
[35] J.i. Liang, Y. Jiao, M. Jaroniec, S.Z. Qiao, Sulfur and nitrogen dual-doped mesoporous graphene electrocatalyst for oxygen reduction with synergistically enhanced performance, Angew. Chem. Int. Edit. 51 (46) (2012) 11496–11500.
[36] T. Zhu, Q. Feng, S. Liu, C. Zhang, Metallogel-derived 3D porous carbon nanosheet composites as an electrocatalyst for oxygen reduction reaction, Compos. Commun. 20 (2020) 100376–100380.
[37] A. Sadezky, H. Muckenhuber, H. Grothe, R. Niessner, U. Pöschl, Raman microspectroscopy of soot and related carbonaceous materials: Spectral analysis and structural information, Carbon 43 (8) (2005) 1731–1742.
[38] D. Qiu, J. Guan, M. Li, C. Kang, J. Wei, F. Wang, R.u. Yang, Cucurbit[6]uril-Derived Nitrogen-Doped Hierarchical Porous Carbon Confined in Graphene Network for Potassium-Ion Hybrid Capacitors, Adv. Sci. 7 (20) (2020) 2001681, https://doi.org/10.1002/advs.v7.2010.1002/advs.202001681.
[39] G. Chao, L. Zhang, J. Tian, W. Fan, T. Liu, Pd–SnO_2 heterojunction catalysts anchored on graphene sheets for enhanced oxygen reduction, Compos. Commun. 25 (2021) 100703.
[40] J. Ma, J. Li, R. Wang, Y. Yang, P. Yin, J. Mao, T. Ling, S. Qiao, Hierarchical porous S-doped Fe–N–C electrocatalyst for high-power-density zinc–air battery, Mater. Today Energy 19 (2021) 100624.
[41] Y. Zheng, S. Chen, K.A.I. Zhang, J. Zhu, J. Xu, C. Zhang, T. Liu, Ultrasound-triggered assembly of covalent triazine framework for synthesizing heteroatom-doped carbon nanoflowers boosting metal-free bifunctional electrocatalysis, ACS Appl. Mater. Interfaces 13 (11) (2021) 13328–13337.
[42] R. Wu, X. Wan, J. Deng, X. Huang, S. Chen, W. Ding, L.i. Li, Q. Liao, Z. Wei, NaCl protected synthesis of 3D hierarchical metal-free porous nitrogen-doped carbon catalysts for the oxygen reduction reaction in acidic electrolyte, Chem. Commun. 55 (61) (2019) 9023–9026.
[43] H. Yang, Y. Wu, Q. Lin, L. Fan, X. Chai, Q. Zhang, J. Liu, C. He, Z. Lin, Composition Tailoring via N and S Co-doping and Structure Tuning by Constructing Hierarchical Pores: Metal-Free Catalysts for High-Performance Electrochemical Reduction of CO2, Angew. Chem., Int. Ed. 57 (47) (2018) 15476–15480.
[44] X. Li, Y. Xu, Y. Li, X. Fan, G. Zhang, F. Zhang, W. Peng, Increasing the heteroatoms doping percentages of graphene by porous engineering for enhanced electrocatalytic activities, J. Colloid and Interf. Sci. 577 (2020) 101–108.
[45] X. Zhang, S. Wang, C. Wu, H. Li, Y.i. Cao, S. Li, H. Xia, Synthesis of S-doped AuPbPt alloy nanowire-networks as superior catalysts towards the ORR and HER, J. Mater. Chem. A 8 (45) (2020) 23906–23918.
[46] Y. Zheng, S. Chen, H. Lu, C. Zhang, T. Liu, 3D honeycombed cobalt, nitrogen co-doped carbon nanosheets via hypersaline-protected pyrolysis towards efficient oxygen reduction, Nanotechnology 31 (36) (2020) 364003, https://doi.org/10.1088/1361-6528/ab97d5.
[47] G. de Falco, M. Florent, A. De Rosa, T.J. Bandosz, Proposing an unbiased oxygen reduction reaction onset potential determination by using a Savitzky-Golay differentiation procedure, J. Colloid and Interf. Sci. 586 (2021) 597–600.
[48] W. Peng, X. Yang, L. Mao, J. Jin, S. Yang, J. Zhang, G. Li, ZIF-67-derived Co nanoparticles anchored in N doped hollow carbon nanofibers as bifunctional oxygen electrocatalysts, Chem. Eng. J. 407 (2021) 127157.
[49] H. Yang, X. Chen, W.-T. Chen, Q. Wang, N.C. Cuello, A. Nafady, A.M. Al-Enizi, G.I. N. Waterhouse, G.A. Goenaga, T.A. Zawodzinski, P.E. Kruger, J.E. Clements, J. Zhang, H.e. Tian, S.G. Telfer, S. Ma, Tunable Synthesis of Hollow Metal–Nitrogen–Carbon Capsules for Efficient Oxygen Reduction Catalysis in Proton Exchange Membrane Fuel Cells, ACS Nano 13 (7) (2019) 8087–8098.
[50] Y. Zheng, S. Chen, H. Song, H. Guo, K.A.I. Zhang, C. Zhang, T. Liu, Nitrogen-doped hollow carbon nanoflowers from a preformed covalent triazine framework for metal-free bifunctional electrocatalysis, Nanoscale 12 (27) (2020) 14441–14447.
[51] Z. Wang, H. Jin, T. Meng, K.e. Liao, W. Meng, J. Yang, D. He, Y. Xiong, S. Mu, Fe, Cu-Coordinated ZIF-Derived Carbon Framework for Efficient Oxygen Reduction Reaction and Zinc-Air Batteries, Adv. Funct. Mater. 28 (39) (2018) 1802596, https://doi.org/10.1002/adfm.201802596.
[52] F. Shi, J. He, B. Zhang, J. Peng, Y. Ma, W. Chen, F. Li, Y. Qin, Y. Liu, W. Shang, P. Tao, C. Song, T. Deng, X. Qian, J. Ye, J. Wu, Plasmonic-Enhanced Oxygen Reduction Reaction of Silver/Graphene Electrocatalysts, Nano Lett. 19 (2) (2019) 1371–1378.
[53] Y. Cheng, Y. Wang, Q. Wang, Z. Liao, N. Zhang, Y. Guo, Z. Xiang, Hierarchically porous metal-free carbon with record high mass activity for oxygen reduction and Zn-air batteries, J. Mater. Chem. A 7 (16) (2019) 9831–9836.
[54] Y. Wang, L.i. Tao, Z. Xiao, R.u. Chen, Z. Jiang, S. Wang, 3D Carbon Electrocatalysts In Situ Constructed by Defect-Rich Nanosheets and Polyhedrons from NaCl-Sealed Zeolitic Imidazolate Frameworks, Adv. Funct. Mater. 28 (11) (2018) 1705356, https://doi.org/10.1002/adfm.v28.1110.1002/adfm.201705356.
[55] J.-J. Cai, Q.-Y. Zhou, X.-F. Gong, B. Liu, Y.-L. Zhang, Y.-K. Dai, D.-M. Gu, L. Zhao, X.-L. Sui, Z.-B. Wang, Metal-free amino acid glycine-derived nitrogen doped carbon aerogel with superhigh surface area for highly efficient Zn-Air batteries, Carbon 167 (2020) 75–84.
[56] Q. Wei, M. Cherif, G. Zhang, A. Almesrati, J. Chen, M. Wu, N. Komba, Y. Hu, T. Regier, T.-K. Sham, F. Vidal, S. Sun, Transforming reed waste into a highly active metal-free catalyst for oxygen reduction reaction, Nano Energy 62 (2019) 700–708.
[57] H.B. Yang, J. Miao, S.-F. Hung, J. Chen, H.B. Tao, X. Wang, L. Zhang, R. Chen, J. Gao, H.M. Chen, L. Dai, B. Liu, Identification of catalytic sites for oxygen reduction and oxygen evolution in N-doped graphene materials: Development

of highly efficient metal-free bifunctional electrocatalyst, Sci. Adv. 2 (4) (2016) e1501122.
[58] Y. Qian, T. An, K.E. Birgersson, Z. Liu, D. Zhao, Web-Like Interconnected Carbon Networks from NaCl-Assisted Pyrolysis of ZIF-8 for Highly Efficient Oxygen Reduction Catalysis, Small 14 (16) (2018) 1704169, https://doi.org/10.1002/smll.v14.1610.1002/smll.201704169.
[59] Y.i. Jia, L. Zhang, A. Du, G. Gao, J. Chen, X. Yan, C.L. Brown, X. Yao, Defect Graphene as a Trifunctional Catalyst for Electrochemical Reactions, Adv. Mater. 28 (43) (2016) 9532–9538.
[60] J. Zhang, Z. Zhao, Z. Xia, L. Dai, A metal-free bifunctional electrocatalyst for oxygen reduction and oxygen evolution reactions, Nat. Nanotechnol. 10 (5) (2015) 444–452.
[61] Q.i. Hu, G. Li, G. Li, X. Liu, B. Zhu, X. Chai, Q. Zhang, J. Liu, C. He, Trifunctional Electrocatalysis on Dual-Doped Graphene Nanorings-Integrated Boxes for Efficient Water Splitting and Zn–Air Batteries, Adv. Energy Mater. 9 (14) (2019) 1803867, https://doi.org/10.1002/aenm.v9.1410.1002/aenm.201803867.
[62] G. Chen, J. Liu, Q. Li, P. Guan, X. Yu, L. Xing, J. Zhang, R. Che, A direct H_2O_2 production based on hollow porous carbon sphere-sulfur nanocrystal composites by confinement effect as oxygen reduction electrocatalysts, Nano Res. 12 (10) (2019) 2614–2622.
[63] H. Wu, Z. Chen, Y. Wang, E. Cao, F. Xiao, S. Chen, S. Du, Y. Wu, Z. Ren, Regulating the allocation of N and P in codoped graphene via supramolecular control to remarkably boost hydrogen evolution, Energy Environ. Sci. 12 (9) (2019) 2697–2705.
[64] G. Chao, L. Zhang, D. Wang, S. Chen, H. Guo, K. Xu, W. Fan, T. Liu, Activation of graphitic nitrogen sites for boosting oxygen reduction, Carbon 159 (2020) 611–616.
[65] X. Yu, Y. Zheng, H. Zhang, Y. Wang, X. Fan, T. Liu, Fast-Recoverable, Self-Healable, and Adhesive Nanocomposite Hydrogel Consisting of Hybrid Nanoparticles for Ultrasensitive Strain and Pressure Sensing, Chemistry of materials 33 (15) (2021) 6146–6157, https://doi.org/10.1021/acs.chemmater.1c01595.
[66] J. Liu, C. Wang, Y. Song, S. Zhang, Z. Zhang, L. He, M. Du, Two-dimensional triazine-based porous framework as a novel metal-free bifunctional electrocatalyst for zinc-air batty 591 (2021) 253–263, https://doi.org/10.1016/j.jcis.2021.02.007.